

Characterization and Surface-Reactivity of Nanocrystalline Anatase in Aqueous Solutions

Moira K. Ridley*

Department of Geosciences, Texas Tech University, Lubbock, Texas 79409-1053

Vincent A. Hackley

Materials Science & Engineering Laboratory, National Institute of Standards & Technology, 100 Bureau Drive, Gaithersburg, Maryland 20899-8520

Michael L. Machesky

Illinois State Water Survey, 2204 Griffith Drive, Champaign, Illinois 61820

Received June 20, 2006. In Final Form: September 19, 2006

The chemical and electrostatic interactions at mineral–water interfaces are of fundamental importance in many geochemical, materials science, and technological processes; however, the effects of particle size at the nanoscale on these interactions are poorly known. Therefore, comprehensive experimental and characterization studies were completed, to begin to assess the effects of particle size on the surface reactivity and charging of metal-oxide nanoparticles in aqueous solutions. Commercially available crystalline anatase (TiO₂) particles were characterized using neutron and X-ray small-angle scattering, electron microscopy, and laser diffraction techniques. The 4 nm primary nanoparticles were found to exist almost exclusively in a hierarchy of agglomerated structures. Potentiometric and electrophoretic mobility titrations were completed in NaCl media at ionic strengths from (0.005 to 0.3) mol/kg, and 25 °C, with these two experimental techniques matched as closely as the different procedures permitted. The pH of zero net proton charge (pH_{znp}, from potentiometric titration) and isoelectric point pH value (pH_{iep}, from electrophoretic mobility titrations) were both in near perfect agreement (6.85 ± 0.02). At high ionic strengths the apparent pH_{znp} value was offset slightly toward lower pH values, which suggests some specific adsorption of the Na⁺ electrolyte ions. Proton-induced surface charge curves of nanocrystalline anatase were very similar to those of larger rutile crystallites when expressed relative to their respective pH_{znp} values, indicating that the development of positive and negative surface charge away from the pH_{znp} for nanocrystalline anatase is similar to that of larger TiO₂ crystallites.

Introduction

Oxide and oxyhydroxide crystals with nanometer-scale dimensions are common in natural systems near the Earth's surface, arising from chemical weathering and as biomineralization products. Moreover, metal oxide nanoparticles are of increasing interest in the material sciences and nanotechnology industry, and more recently to toxicologists. In each discipline, awareness and interest in nanometer particles arises from the unique physiochemical properties of these materials that change as a function of particle size in the nanoscale domain.

Nanosized particles are ubiquitous at the Earth's surface.^{1–3} Furthermore, nanoparticles may play a considerable role in biogeochemical and environmental processes. For example, Madden and Hochella⁴ noted that the magnitude of manganese oxidation varies as a function of hematite particle-size at the nanoscale. Similarly, there have been several recent studies examining the fate and transport of nanosized iron-particles, which are of particular environmental concern as they may adsorb and desorb a range of radionuclide, and heavy and toxic metals.^{5–9}

Engineered metal-oxide nanomaterials are used extensively as catalysts and in a variety of commercial products and applications. In particular, titanium dioxide (TiO₂) nanoparticles have been employed as photocatalysts, in sunscreens and paints, and in environmental remediation.^{10–16} In most applications, the small particle size, tunable properties, and large and accessible surface areas of the engineered TiO₂ nanomaterials has been advantageous. However, these desirable technological traits may be offset by increased toxicological and other environmental risks.^{17–20}

* Corresponding author: E-mail: moira.ridley@ttu.edu.

(1) Banfield, J. F.; Zhang, H. In *Nanoparticles and the environment*; Banfield, J. F., Navrotsky A., Eds.; Reviews in mineralogy and geochemistry, 2001; Vol. 44, pp 1–58.

(2) Gibb, A. A.; Banfield, J. F. *Am. Mineral.* **1997**, *82*, 717–729.

(3) Smith, K. L.; Milnes, A. R.; Eggleton, R. A. *Clays Clay Miner.* **1987**, *35*, 418–428.

(4) Madden, A. S.; Hochella, M. F. *Geoch. Cosmochim. Acta* **2005**, *69*, 389–398.

(5) Gao, Y.; Wahi, R.; Kan, A. T.; Falkner, J. C.; Colvin, V. L.; Tomson, M. B. *Langmuir* **2004**, *20*, 9585–9593.

(6) Hochella, M. F.; Kasama, T.; Putnis, A.; Putnis, C. V.; Moore, J. N. *Am. Mineral.* **2005**, *90*, 718–724.

(7) Schemel, L. E.; Kimball, B. A.; Bencala, K. E. *Appl. Geochem.* **2000**, *15*, 1003–1018.

(8) Um, W.; Papelis, C. *Environ. Geol.* **2002**, *43*, 209–218.

(9) Waychunas, G. A.; Kim, C. S.; Banfield, J. F. *J. Nanoparticle Res.* **2005**, *7*, 409–433.

(10) Bell, A. T. *Science* **2003**, *299*, 1688–1701.

(11) Chen, L. X.; Rajh, T.; Jäger, W.; Nedeljkovic, J.; Thurnauer, M. C. *J. Synchrotron Radiation* **1999**, *6*, 445–447.

(12) Choi, W.; Termin, A.; Hoffmann, M. R. *J. Phys. Chem.* **1994**, *98*, 13669–13679.

(13) Kormann, C.; Bahnemann, D. W.; Hoffmann, M. R. *Environ. Sci. Technol.* **1991**, *25*, 494–500.

(14) Masciangelo, T.; Zhang, W. X. *Environ. Sci. Technol.* **2003**, *37*, 102A–108A.

(15) Ohno, T.; Mitsui, T.; Matsumura, M. *J. Photochem. Photobiol. A: Chemistry* **2003**, *160*, 3–9.

(16) Zhang, H.; Banfield, J. F. *Chem. Mater.* **2005**, *17*, 3421–3425.

(17) Colvin, V. *Nat. Biotechnol.* **2003**, *21*, 1166–1170.

(18) Diallo, M. S.; Savage, N. *J. Nanoparticle Res.* **2005**, *7*, 325–330.

In addition to unique physical and chemical properties, the large surface area of nanoscale particles likely changes the surface reactivity of the particles as a function of particle size. As the size of nanoparticles decrease, a greater proportion of the atoms present exist at the surface,^{19,21} increasing the ratio of unsatisfied surface bonds relative to the bulk oxygen–metal bonds. Furthermore, the large curvature of particles may modify the surface relaxation of surface oxygen atoms or change the coordination geometry of surface atoms. For example, Chen et al.¹¹ and Rajh et al.^{22,23} suggest that the Ti–O coordination geometry of TiO₂ crystallites changes with particle size especially for particles less than about 2 nm in diameter. Moreover, the area of particle edges also increases with decreasing particle size, and molecular dynamics simulations have suggested that these edges are regions of preferential charge accumulation presumably because these areas are more effectively solvated.²⁴

It is already well established for macroscopic metal-oxide particles that terminal oxygen atoms react with water, forming hydroxylated surface-functional groups that impart a pH-dependent surface charge on the oxide phase, resulting in the development of an electric potential gradient between the metal-oxide surface and the bulk solution, namely the electric double layer (EDL). The EDL influences all interfacial processes including, catalysis, crystal growth, colloid transport and flocculation, adsorption of ions from solution, mineral corrosion/dissolution/precipitation, and other interfacial reactions. For example, it has already been demonstrated that nanoparticle size is tightly coupled to particle surface charge, which can be controlled through the pH and ionic strength of the precipitating medium.^{25,26} Moreover, if the surface characteristics and ion-coordination/geometry of nanoscale metal-oxide particles indeed change with particle size, then this may result in different surface reactivity and charging behavior, including different pH values for the point of zero net proton charge (pH_{znpc}) and isoelectric pH (pH_{iep}) relative to macroscopic crystals. In that case, data describing the surface behavior of macroscopic crystals^{27–33} may not be directly applicable to nanometer-sized crystals.

This manuscript presents the results of detailed experimental and characterization studies of commercially available 4 nm anatase (TiO₂) crystallites in aqueous solutions. These studies were conducted to quantitatively evaluate the surface charging

behavior and to determine the pH_{znpc} and pH_{iep} values of nanocrystalline anatase. The nanoparticles were characterized using neutron and X-ray small-angle scattering, electron microscopy, and laser diffraction techniques in order to determine the size and structure of both the primary crystallites and their aggregates. The surface charging properties of the nanoparticles in aqueous solutions were then investigated by potentiometric and electrophoretic mobility titrations, which were matched as closely as the different procedures permitted. A sonication step preceded these titration procedures since it was shown to improve the reproducibility of the titrations. These detailed characterization procedures, which focus on defining the surface properties of nanocrystalline anatase in aqueous solutions, constitute an important first step in efforts to quantify the effects of particle size on surface reactivity.

Experimental Methods

Materials. The anatase (designated ST-01) used in all experiments was obtained from Ishihara Techno Corporation, Osaka, Japan.³⁴ Prior to use, the anatase was subjected to repeated washing–centrifuging cycles in distilled–deionized water. This initial washing was essential to ensure that the surface of the particles were largely free of synthesis procedure residues and other potential water-soluble impurities. For all washing cycles, the pH of the supernate was >5 and conductivity was low, suggesting that water-soluble impurities were low in the as-received powder. In our earlier work with rutile (TiO₂), the powders were rinsed by numerous washing–boiling–decantation cycles, followed by hydrothermal aging.^{29,35} However, such rigorous treatment of the ST-01 powder resulted in surface-charge titration curves becoming very ‘noisy’ and irreproducible. Similarly, not washing the ST-01 powder also resulted in ‘noisy’ data as well as titration hysteresis.

All potentiometric titration solutions were prepared from reagent-grade chemicals and deionized water. The general method used to prepare and store the calibration, solid-dispersion and titrant solutions has been described previously.^{29,36} All solutions were prepared at five ionic strengths (0.005, 0.01, 0.03, 0.06, and 0.3 *m*, where *m* is used throughout this paper to indicate aqueous concentration in units of molality, moles of solute per kilogram of water). The initial electrode calibration solution was basic, comprising 5 × 10^{−4} *m* NaOH (see potentiometric titration procedure given below), to which an acid calibration solution containing sufficient HCl to attain a calibration point close to 0.002 *m* H⁺ was added. The solid-dispersion solutions at 0.005 *m* and 0.01 *m* ionic strength comprised 6 × 10^{−4} *m* HCl, whereas solutions at >0.01 *m* ionic strength comprised 0.002 *m* HCl. In all solid-dispersion solutions, sufficient NaCl was added to produce the desired ionic strength. The titrant solutions comprised NaOH and NaCl; as in previous studies^{29,30,37} the ionic strength of the titrant was slightly higher than the corresponding calibration and dispersion solutions, making it possible to largely compensate for changes in ionic strength during a titration. Consequently, the ionic strength varied no more than 2.5% throughout a particular titration; however, the deviation approached 5% for titrations performed at 0.005 *m* ionic strength.

The experimental solutions for the electrophoretic mobility titrations were prepared from NIST-traceable titrants, including HCl (0.5 mol/L) and low-carbonate NaOH (0.5 and 0.1 mol/L), obtained from EM Science (Gibbstown, NJ). Base titrants were stored under argon after opening. Analytical grade NaCl crystals were obtained

(19) Nel, A.; Xia, T.; Mädler, L.; Li, N. *Science* **2006**, *311*, 622–627.

(20) Oberdörster, G.; Oberdörster, E.; Oberdörster, J. *Environ. Health Perspect.* **2005**, *113*, 823–839.

(21) Klabunde, K. J. In *Nanoscale materials in chemistry*; Klabunde, K. J., Ed.; Wiley Inter-Science, 2001; pp 1–13.

(22) Rajh, T.; Chen, L. X.; Lukas, K.; Liu, T.; Thurnauer, M. C.; Tiede, D. *M. J. Phys. Chem. B* **2002**, *106*, 10543–10552.

(23) Rajh, T.; Nedeljkovic, J. M.; Chen, L. X.; Poluektov, O.; Thurnauer, M. C. *J. Phys. Chem. B* **1999**, *103*, 3515–3519.

(24) Rustad, J. R.; Felmy, A. R. *Geoch. Cosmochim. Acta* **2005**, *69*, 1405–1411.

(25) Jolivet, J.-P.; Froidefond, C.; Pottier, A.; Chanéac, C.; Cassaignon, S.; Tronc, E.; Euzen, P. *J. Mater. Chem.* **2004**, *14*, 3281–3288.

(26) Pottier, A.; Cassaignon, S.; Chanéac, C.; Villain, F.; Tronc, E.; Jolivet, J.-P. *J. Mater. Chem.* **2003**, *13*, 877–882.

(27) Fenter, P.; Cheng, L.; Rihls, S.; Machesky, M. L.; Bedzyk, M. J.; Sturchio, N. C. *J. Colloid Interface Sci.* **2000**, *225*, 154–165.

(28) Hiemstra, T.; Van Riemsdijk, W. H. In *Encyclopedia of Colloid and Interface Science*; Hubbard, A. T., Ed.; Marcel Dekker: New York, 2002; pp 3773–3799.

(29) Ridley, M. K.; Machesky, M. L.; Palmer, D. A.; Wesolowski, D. J. *Colloids Surf., A* **2002**, *204*, 295–308.

(30) Ridley, M. K.; Wesolowski, D. J.; Palmer, D. A.; Kettler, R. M. *Geoch. Cosmochim. Acta* **1999**, *63*, 459–472.

(31) Sverjensky, D. *Geoch. Cosmochim. Acta* **2005**, *69*, 225–257.

(32) Van Damme, H. In *Adsorption on Silica Surfaces, Surfactant Science Series*; Papirer, E., Ed.; Marcel Dekker: New York, 2000; Vol. 90, pp 119–166.

(33) Zhang, Z.; Fenter, P.; Cheng, L.; Sturchio, N. C.; Bedzyk, M. J.; Pøedota, M.; Bandura, A.; Kubicki, J.; Lvov, S. N.; Cummings, P. T.; Chialvo, A. A.; Ridley, M. K.; Bénézech, P.; Anovitz, L.; Palmer, D. A.; Machesky, M. L.; Wesolowski, D. J. *Langmuir* **2004**, *20*, 4954–4969.

(34) Certain trade names and company products are mentioned in the text or identified in illustrations in order to specify adequately the experimental procedure and equipment used. In no case does such identification imply recommendation or endorsement by the National Institute of Standards and Technology, nor does it imply that the products are necessarily the best available for the purpose.

(35) Machesky, M. L.; Wesolowski, D. J.; Palmer, D. A.; Hayashi, K.-I. *J. Colloid Interface Sci.* **1998**, *200*, 298–309.

(36) Palmer, D. A.; Wesolowski, D. J. *Geoch. Cosmochim. Acta* **1993**, *57*, 2929–2938.

(37) Ridley, M. K.; Machesky, M. L.; Wesolowski, D. J.; Palmer, D. A. *Geoch. Cosmochim. Acta* **2005**, *69*, 63–81.

from Mallinckrodt (St. Louis, MO). Solutions were prepared at 0.01, 0.03 and 0.3 *m*. NIST-traceable pH buffers from Fisher Scientific (Pittsburgh, PA) were used for the calibration of the pH meter.

Characterization of Anatase. The nanometer anatase powder was characterized extensively using high-resolution transmission electron microscopy (HR-TEM), X-ray diffraction (XRD), thermogravimetric analysis (TGA), and Brunauer–Emmett–Teller (BET) N₂-adsorption surface area measurements. The XRD results verified that the TiO₂ sample used in this study was pure, crystalline anatase. No other crystalline TiO₂ phases (specifically, brookite and rutile) were identified. To better determine particle size, small-angle neutron scattering (SANS), ultra-small-angle X-ray scattering (USAXS), and laser diffraction measurements were also completed.

Small-angle neutron scattering measurements were performed using a pinhole collimated 30 m SANS instrument³⁸ on the NG-7 guide at the NIST Center for Neutron Research, over a scattering vector, Q , range from 0.00089 Å⁻¹ to 0.505 Å⁻¹ (where $Q = 2\pi/\lambda \sin\theta$ and 2θ is the scattering angle). The neutron wavelength was 6 Å with a resolution $\Delta\lambda/\lambda = 0.11$, and the sample aperture was 1.27 cm. Dry powder was loaded between two quartz windows in a demountable cell with a 1 mm path length. To obtain data over the maximum Q range, each sample was measured in three instrument configurations with nominal sample-to-detector distances of 1.0, 15, and 15.3 m (the latter with neutron focusing lens). Data were collected using a (64 × 64) cm position sensitive proportional counter and circularly averaged to obtain the isotropic scattered intensity, $I(Q)$. Scattering was corrected for detector efficiency, background and parasitic scattering.

Ultra-small-angle X-ray scattering measurements were performed using the double-crystal Bonse-Hart instrument^{39,40} at the UNICAT facility, 33-ID beam line, Advanced Photon Source, Argonne National Laboratory. A suspension containing a mass fraction of 0.74% (0.19% volume fraction) anatase powder was dispersed ultrasonically in deionized water preadjusted to pH 10.5 with NaOH. The final suspension pH was 10.7. The suspension was placed in a custom built capillary flow-cell.⁴¹ Scattered intensity was measured in slit-smear collimation using 10.76 keV X-rays. The measured scattering curve was corrected for background/matrix scattering by subtracting an appropriate solution blank and then desmeared using the Lake algorithm.⁴²

Laser diffraction measurements were performed on a Coulter LS-230 laser diffraction instrument (Beckman Coulter Inc., Hialeah, FL). For these measurements a stock suspension of anatase powder at a mass concentration of 200 mg/kg was prepared in deionized water previously acidified to pH 2.7 with HCl. The stock suspension was dispersed using a 450 W ultrasonicator. The LS-230's reservoir was filled with a pH 2.7 HCl solution, which was recirculated constantly. The anatase-stock suspension was added to the reservoir dropwise until an optimum obscuration level was achieved. Prior to each measurement, the reservoir suspension was ultrasonicated for 4 min using the instrument's built-in low intensity ultrasonicator. Five consecutive measurements were performed, a fresh dispersion was prepared from the anatase-stock suspension as described above, and five additional measurements were completed. The Mie optical model, with a refractive index value of 2.55, was employed to calculate size distributions from the angular-resolved diffraction data. The distributions for the 10 runs were averaged to produce a mean curve with vertical bars representing one standard deviation. The data are presented as the differential volume % versus particle diameter.

(38) Glinka, C. J.; Barker, J. G.; Hammouda, B.; Krueger, S.; Moyer, J. J.; Orts, W. J. *J. Appl. Crystallogr.* **1998**, *31*, 430–445.

(39) Long, G. G.; Allen, A. J.; Ilavsky, J.; Jemian, P. R.; Zschack, P. In *Synchrotron Radiation Instrumentation*. Proceedings of the 11th U.S. National Conference, Stanford, CA, Oct 13–15, 1999; Pianetta, P., Arthur, J., Brennan, S., Eds.; American Institute of Physics: Melville, NY, 2000; Vol. 521, pp 183–187.

(40) Long, G. G.; Jemian, P. R.; Weertman, J. R.; Black, D. R.; Burdette, H. E.; Spal, R. *J. Appl. Crystallogr.* **1991**, *24*, 30–37.

(41) Hackley, V. A.; Allen, A. J.; Jemian, P. R.; Raitano, J. M.; Chan, S.-W. In *Proceedings of the Fifth World Congress on Particle Technology*; AIChE: New York, 2006.

(42) Lake, J. A. *Acta Crystallogr.* **1967**, *23*, 191–194.

Potentiometric Titration Procedure. The experimental system for potentiometric titrations utilized a Mettler DL70 autotitrator and Ross Semimicro combination glass-electrodes. For each titration approximately 0.04 g of anatase was suspended in 16 g of dispersing solution, at the ionic strength of interest. The anatase was dispersed using a high intensity (750 W) ultrasonicator with an immersible titanium horn. During sonication, the cavitation intensity was increased from 40 % to 60 % in cycles alternating between 15 s of cavitation and 60 s with no power, over 7 min. This cycling procedure was optimized to minimize sample heating and to prevent adversely altering the samples. The maximum temperature reached during sonication was 47.3 °C. The dispersed sample was transferred to the titration cell, and an additional 24 g of dispersing solution was added, totaling 40 g of dispersion solution. The sample mass used in each titration provided at least 12 m² of surface area, which gave sufficiently large pH effects for accurate proton balance calculations.

The titration cell was sealed and immersed in a water bath at 25 °C (±0.1 °C), and the headspace was purged with argon to prevent CO₂ contamination; furthermore, the solutions were stirred mechanically at all times. The anatase test solution was then allowed to equilibrate for at least 1 h at temperature before starting the titrations. Equilibration of the anatase test solution was assumed when the potential drift (monitored every 10 s throughout the titration) was <0.1 mV over at least 6 min. The equilibration criteria were typically met within 30 min; thereafter, the cell potential remained stable until the titration commenced. Conversely, if the dispersion step was omitted or inadequate, the cell potential would drift indefinitely: explicitly, equilibration of the test solution was never obtained. The titrations proceeded by equilibrating a Ross combination electrode in 36 g of basic calibration solution, at 25 °C (± 0.1 °C). Once a stable potential was attained (i.e. a drift rate <0.05 mV/min), 4 g of acid calibration solution was titrated into the cell, giving a proton concentration close to that of the dispersing solution. These two readings were used to calibrate the electrode and define the operational Nernst slope, as described below. Following calibration, the electrode was rapidly transferred to the anatase test solution, whereupon the titration proceeded in a conventional manner by the addition of a basic titrant. Each addition of titrant produced a change in potential of approximately 15 mV. At low pH conditions, the cell potential reequilibrated to a potential drift rate of <0.05 mV/min within 5 min; however, as pH increased to between 6 and 8, equilibration required the maximum 10 min permitted by the Mettler DL70 system. In total 30 to 35 aliquots of titrant were added, over a pH_m range of approximately 7 units (where, pH_m is the negative logarithm of hydrogen ion molality⁴³). The titrations were terminated when the measured cell potential exceeded the calibration range. Titrations were completed in approximately 4 h, which was sufficiently rapid to limit the growth and aggregation, or dissolution of the nanoparticles. Each titration yielded a single set of acid-to-base titration data for a specific ionic strength. Titrations can then be reversed (back-titrated) by adding acidic titrant, which was only completed in a few instances to determine the presence/absence of titration hysteresis.

Instrumentation for the Electrophoretic Mobility Titrations.

Electrophoretic mobility measurements were conducted using a ZetaSizer 3000HS laser-Doppler device from Malvern Instruments Inc. (Southborough, MA). This instrument uses a 5 mW He–Ne laser and single photon detection to determine the Doppler-shifted spectrum of light scattered from particles moving under the influence of an applied d.c. electric field. The detected signal is analyzed by an autocorrelation method to determine the frequency spectrum. In this instrument, the laser beam is split and one portion reflected from a mirror attached to a piezoelectric modulator. The modulated beam provides a measurable Doppler shift even for particles at rest (zero mobility), thereby permitting high resolution measurements in the vicinity of the isoelectric point (IEP). The modulation also provides an absolute determination of particle polarity. Mobility measurements were taken at the hydrodynamic stationary layer within the rectangular quartz capillary cell. The direction of the applied

(43) Mesmer, R. E.; Holmes, H. F. *J. Sol. Chem.* **1992**, *21*, 725–744.

field was reversed at 1 s intervals to avoid electrode polarization. A zero-field correction was made for each measured spectrum to account for broadening due to Brownian motion. The reported electrophoretic mobility (particle velocity per applied electric field strength) represents the mean of the measured mobility spectrum. Correct operation of the instrument was validated periodically using SRM 1980 and Malvern transfer standard DTS1050 (traceable to SRM 1980).⁴⁴

A Metrohm combination glass electrode (Brinkman Instruments, Westbury, NY), with 3 mol/L KCl filling solution, and a Thermo Orion pH/ISE meter were used. An ATC probe was used in conjunction with the pH electrode to monitor temperature in the sample cell. Titrations were conducted manually using a custom built thermal-jacketed titration apparatus.

Electrophoretic Mobility Titration Procedure. A test suspension was prepared by adding 0.06 g anatase to 400 g electrolyte solution, which had been preadjusted to pH 2.7 in an acid cleaned Teflon container. This suspension yielded a solid concentration of 150 mg/kg solution. As for the potentiometric titrations, the sample was dispersed using a high intensity (450 W) ultrasonicator with an immersible titanium horn, which was pulsed using a 50% duty-cycle for 6 min. The sample cell was then mounted on the titration apparatus and sealed and the headspace flushed with N₂ gas to maintain a positive pressure throughout the titration. Furthermore, the sample was stirred continuously using a Teflon-coated magnetic stir bar, and temperature was maintained at 25 °C (±0.1 °C). The sample was equilibrated for a period of about 1 h, after which pH was monitored for several minutes. A significant pH drift (>0.005 pH units over a 90 s interval) was not observed for any test suspensions following equilibration.

Starting from an initial pH near 2.7, the test suspensions were titrated with NaOH to a pH of 10.3. Nominally 20 data points were obtained for each titration curve over a period of about 3 h. The criteria used to establish equilibrium between each addition of base titrant was a pH drift of less than 0.005 pH units over a 90 s period. A maximum equilibration time of 10 min was allowed for each data point. Between pH 2.7 and pH 5.5, the electrode response stabilized in less than 4 min; however, between pH 5.5 and pH 9 the response drifted for periods up to, and occasionally exceeding, 10 min. Above pH 9, stability was achieved in under 10 min.

Prior to starting a titration, the microelectrophoresis cell was conditioned for at least 10 min using an electrolyte solution identical in composition to the suspension medium. For each data point, 10 mL of test suspension was extracted through a sampling port on the titration cell using a polypropylene syringe with an attached large-bore stainless steel needle. Approximately half the syringe volume was immediately injected into the capillary cell. After 10 s, the remaining suspension was injected, and after an additional 20 s interval, the measurement process was initiated. For each data point, three consecutive mobility measurements were averaged and the standard deviation reported. The pH electrode response was recorded immediately before the first measurement began and again at the conclusion of the final measurement. These two pH values were averaged, and the resulting standard deviation was used to represent a combination of pH drift and measurement precision associated with each mobility data point.

Data Reduction

Potentiometric Titrations. The base and acid calibration points were used to establish the Nernst slope and calibrate the Ross electrode. Specifically, the operational Nernst slope was calculated from the known stoichiometric proton concentrations of the base, [H⁺_{base}], and acidic, [H⁺_{acid}], titrant, and the corresponding potential readings, *E*_{base} and *E*_{acid}, respectively;

$$\text{operational Nernst slope} = (E_{\text{acid}} - E_{\text{base}} + \Delta E_{\text{lj}}) / (\log [H^+]_{\text{acid}} - \log [H^+]_{\text{base}}) \quad (1)$$

where ΔE_{lj} is the difference in calculated liquid junction potentials of the acid and base calibration points relative to the electrode filling solution. The value of [H⁺_{base}] is calculated from the water dissociation constant in NaCl media.⁴⁵ The operational Nernst slope was typically within 1.5% of the theoretical value ($-2.3026RT/F = -59.16 \text{ mV}$ at 25 °C) at ionic strengths >0.005 *m*, and within 2.5% of the theoretical value at 0.005 *m* ionic strength. Having established the operational Nernst slope, eq 1 can be rearranged to,

$$[H^+]_{\text{test}} = [H^+]_{\text{acid}} \times 10^{(E_{\text{acid}} - E_{\text{test}} + \Delta E_{\text{lj}}) / (\text{operational Nernst slope})} \quad (2)$$

and then used to compute the hydrogen ion concentration [H⁺_{test}] at each point in the titration, *E*_{test}. In eq 2 and throughout the titration, the liquid junction potential was calculated relative to the proton concentration [H⁺_{acid}] of the second calibration point, which was chosen as the reference concentration. The liquid junction potential correction is based on the Henderson equation (eq 2–12 in Baes and Mesmer⁴⁶), which gives a conservative estimated error of ±20%. The Henderson equation requires limiting equivalence conductances for all ions in solution; these data were taken from Quist and Marshall.⁴⁷ For all titrations the maximum calculated liquid junction potential was 0.65 mV (in a titration at 0.005 *m* ionic strength), which corresponds to an uncertainty in the calculated pH of less than 0.02 units.

Solution ionic strengths were calculated assuming complete dissociation of the NaCl media, and molal equilibrium concentration quotients were defined for protolytic reactions that were sufficiently strong to be readily measurable, such as the dissociation of water. Moreover, the measured hydrogen ion concentration, [H⁺_{test}], equates to pH_m, which was converted to the activity scale of pH by assuming that the stoichiometric molal activity coefficient of H⁺ in the test solution could be approximated by

$$\gamma_{\text{H}^+} = (\gamma_{\text{H}^+} \gamma_{\text{OH}^-})^{1/2} = (a_{\text{H}_2\text{O}} \times K_w / Q_w)^{1/2} \quad (3)$$

where for the dissociation of water, $Q_w \equiv [H^+][OH^-]$ is the stoichiometric molal equilibrium quotient in a specific ionic medium and approaches the thermodynamic equilibrium constant $K_w \equiv a_{\text{H}^+} a_{\text{OH}^-} / a_{\text{H}_2\text{O}}$ at infinite dilution.

The stoichiometric proton concentration may be calculated for each point of the titration (i.e., [H⁺] in the absence of the solid phase) and compared with the measured [H⁺_{test}] value. Excess H⁺ in solution is assumed to have arisen from the dissociation of protonated surface groups (or the sorption of OH⁻ onto the surface). Conversely, H⁺ “missing” from solution is assumed to have sorbed onto the mineral surface (or to have been neutralized by OH⁻ released from the surface). The micromoles of “excess” or “missing” protons in the test solution at each point in the titration, divided by the total surface area of solid exposed to the experimental solution, may be converted to proton-induced surface charge via the relationship

$$\text{“solution excess or deficit” } \mu\text{mols H}^+/\text{m}^2 \cdot (-F) = \sigma_{\text{H}} \quad (4)$$

(45) Busey, R. H.; Mesmer, R. E. *J. Chem. Eng. Data* **1978**, *23*, 175–176.

(44) Hackley, V. A.; Premachandran, R. S.; Malghan, S. G.; Schiller, S. B. *Colloids Surf. A* **1995**, *98*, 209–224.

(46) Baes, C. F., Jr.; Mesmer, R. E. *The Hydrolysis of Cations*; Krieger: Malabar, FL, 1976; p 489.

(47) Quist, A. S.; Marshall, W. L. *J. Phys. Chem.* **1965**, *69*, 2984–2987.

where σ_H is the proton-induced surface charge density in Coulombs/m² and F is the Faraday constant (0.096494 Coulombs/ μ -equivalent). The negative sign before F in eq 4 indicates that excess H⁺ in solution corresponds to a deficit on the mineral surface (or an excess of OH⁻), giving a negative proton-induced surface charge. Conversely, a deficit of H⁺ in solution, defined as a negative quantity in eq 4, results in a positive calculated surface charge density.

The proton-induced surface charge, as calculated in eq 4, applies only if no additional proton-producing or -consuming side reactions occur, and that the test solution composition can be calculated sufficiently accurately from the dispersing/ starting solution and titrant masses and compositions and the measured pH. The glass surface of the titration cell and the Ross electrode might adsorb H⁺ or OH⁻, and the starting solutions might contain trace levels of protolytic impurities that contribute erroneously to the proton balance calculations. In our previous surface titration studies of macroscopic TiO₂ (rutile) particles, such effects were trivial.²⁹ Moreover, the very high surface area (308 m²/g) of our nano-anatase particles will further minimize such effects, given that the surface area appears in the denominator of eq 4.

Electrophoretic Mobility Titrations. Two methods were used to determine the IEP value. The data were fit with a five-parameter sigmoid (logistic) equation with a 1/ y weighting for each individual titration and for the results of three or more replicate titrations combined for each electrolyte concentration. R^2 values were calculated for each fit; R^2 values for combined data sets equaled or exceeded 0.99. The isoelectric point (IEP) for each electrolyte concentration was then determined from the fitted titration curve. It was found that IEP values determined by averaging results from individual runs and those determined by fitting the combined data sets differed by 0.02 pH units or less. The fits obtained when combining titration data at each ionic strength were considered a more accurate assessment of the IEP values, since the overall shape of the sigmoid curve was better established and the few near-IEP data points were not over-weighted.

Zeta Potential Calculation. The zeta potential can be calculated from the measured mobility using various relationships, but certain assumptions must be made in order to perform this conversion. It is important to note that this conversion does not impact, nor is it necessary, for determination of the IEP as described above.

For the thin EDL approximation ($\kappa a \gg 1$, where $1/\kappa$ is the Debye screening length), the drag force on the particle is entirely due to electrophoretic retardation: the ions surrounding the particle move in the opposite direction, dragging the fluid with them. In this case, the Smoluchowski formula can be applied to particles of arbitrary shape, provided the zeta potential is not very large. At 25 °C in aqueous solution the Smoluchowski limit yields:

$$\zeta \text{ (mV)} = \mu_E \times 12.804 \quad (5)$$

where μ_E is in standard mobility units ($\mu\text{m cm V}^{-1} \text{s}^{-1}$). The Hückel limit for very small κa (i.e., the thick EDL approximation) is not reached at the ionic strength levels used in the present work.

The Smoluchowski limit can be applied to ST-01 if we assume that the particles being detected in the mobility measurements are predominantly micrometer-size aggregates, a premise supported by the physical characterization data (discussed below). If, on the other hand, we choose the primary crystallite size for determination of κa , then the NaCl molalities used here yield intermediate values of κa between the two limits. We have,

therefore, calculated zeta potential using both the thin EDL formula and the analytical solution to the exact equations of O'Brien and White.⁴⁸ The OW calculation requires input of the particle radius and the equivalent conductance for each ionic species present. For these calculations we used 2.2 nm for the particle radius; the results are not overly sensitive to small variations in the radius chosen for these calculations, so 2.2 nm will adequately represent the primary crystallite size and is within the range of values derived from different measurement techniques and laboratories as reported below.

An additional consideration is the potential impact that intraaggregate porosity can have on the measured mobility of ST-01. Previously discussed treatments assume a solid dielectric (nonconducting) particle, but physical characterization results (discussed below) suggest that ST-01 is highly aggregated even in the dispersed state. To assess the magnitude of this effect we have applied the theoretical treatment of Miller et al.⁴⁹ that describes the effect of porosity on the electrophoretic mobility of a uniformly packed assembly of dielectric spheres and expands on the earlier work of Levine and Neale.⁵⁰ Their analysis considers two opposing effects: (1) the presence of conducting electrolyte solution in the aggregate interior, which reduces the tangential component of the electric field and thereby reduces the aggregate mobility compared to a solid dielectric sphere, and (2) the electroosmotic flow through the pore channels of the aggregate, which causes a "jetting" effect that increases aggregate mobility. In this analysis we assume that $a \ll R$, where a is the radius of the primary particles comprising the aggregate, and R is the aggregate external radius. Additionally, we assume $\kappa R \gg 1$, such that the Smoluchowski formula can be applied to the exterior interface of the aggregate. Physical data supports these assumptions, with R of order 1 μm and $R/a \geq 200$. The theoretical treatment is generally applicable to particles with small ζ (≤ 25 mV) and negligible surface conductivity. We employ the constant surface potential assumption for EDL overlap within the pore structure, which yields the following equation describing the dependence of ζ on mobility for a porous aggregate:

$$\zeta = \frac{6\eta\mu_E}{\epsilon(3 - \gamma)(2 + F)} \quad (6)$$

where γ is the intraaggregate porosity and F is an electroosmotic flow factor that is proportional to the velocity of the fluid through the pore channels. The equations describing F are complex and contain integrals, but Levine and Neale⁵⁰ published curves for specific values of $\phi = 1 - \gamma$ as a function of κa , from which we have interpolated values of F corresponding to our experimental system with $\gamma = 0.7$ (see below).

Physical Characterization Results

The measured physical characteristics of ST-01 are summarized in Table 1, along with previously reported values for comparison. Characterization results of ST-01 are described in detail in the following paragraphs.

Thermogravimetric Analysis and Nitrogen Adsorption–Desorption Isotherms. A crucial variable in all surface-charge studies is the surface area of the mineral phase being investigated. Routinely, surface area is determined by N₂-BET measurements. However, obtaining accurate and reproducible

(48) O'Brien, R. W.; White, L. R. *J. Chem. Soc., Faraday Trans. 2* **1978**, *74*, 1607–1626.

(49) Miller, N. P.; Berg, J. C.; O'Brien, R. W. *J. Colloid Interface Sci.* **1992**, *153*, 237–243.

(50) Levine, S.; Neale, G. H. *J. Colloid Interface Sci.* **1974**, *47*, 520–529.

Table 1. Summary of Measured and Reported Physical Characteristics for ST-01 Anatase Powder

BET Specific Surface Area	
source	value (m ² /g)
this study	308.6 ± 2
Ishihara Techno Corporation ^a	320
Almquists and Biswas ^b	300
Nosaka et al. ⁵²	320
Ohno et al. ¹⁵	192.5
BJH Mesopore Volume	
source	value (cm ³ /g)
this study	
adsorption branch	0.59
desorption branch	0.61
Size Parameters	
source	value (nm)
this study	
BET equivalent spherical diameter	5.0 ^c
HR-TEM diameter	4.6
USAXS and SANS primary particle size mode	3.7
laser diffraction median diameter	2329
Ishihara Techno Corporation ^a	
XRD (Scherrer formula) crystallite size	7
Almquists and Biswas ⁵¹	
BET equivalent spherical diameter	5.0
XRD (Scherrer formula) crystallite size	8
Nosaka et al. ⁵²	7

^a Ishihara Techno Corporation, product data sheet. ^b Almquists and Biswas,⁵¹ BET degassing temperature 150 °C, sample used as-received. ^c BET equivalent spherical diameter calculated using a density of 3.89 g/cm³.

surface area measurements of nanoscale particles is commonly problematic,⁵³ because the measured surface area may be dependent on the degassing temperature and procedure that is followed. An estimate for the most appropriate BET degassing temperatures may be gained from TGA measurements, thus permitting accurate and reproducible surface area measurements to be made. Thermogravimetric analysis was conducted by heating the anatase sample from 35 °C to 200 °C at a rate of 5 °C/min, then from 200 °C to 285 °C at a rate of 10 °C/min (Figure 1). This temperature interval corresponds to the range of typical BET degassing temperatures. The upper curve in Figure 1 shows the weight loss as a function of temperature and the lower curve is its derivative. The total weight loss over the interval measured was 7.6%. The derivative curve shows a marked change in slope at roughly 125 °C; the curve then plateaus to 220 °C. The weight loss between 35 °C and 125 °C was 4.6%. Reproducible BET surface area measurements were obtained when a degassing temperature of 125 °C was used. During degassing, the temperature was increased from room temperature to 125 °C in 15 °C increments, with each temperature increment maintained for (15 to 20) min. Degassing at temperatures less than 125 °C or above 200 °C resulted in lower surface areas. The N₂-BET surface area of the cleaned sample used in most titrations was (308.6 ± 2) m²/g.

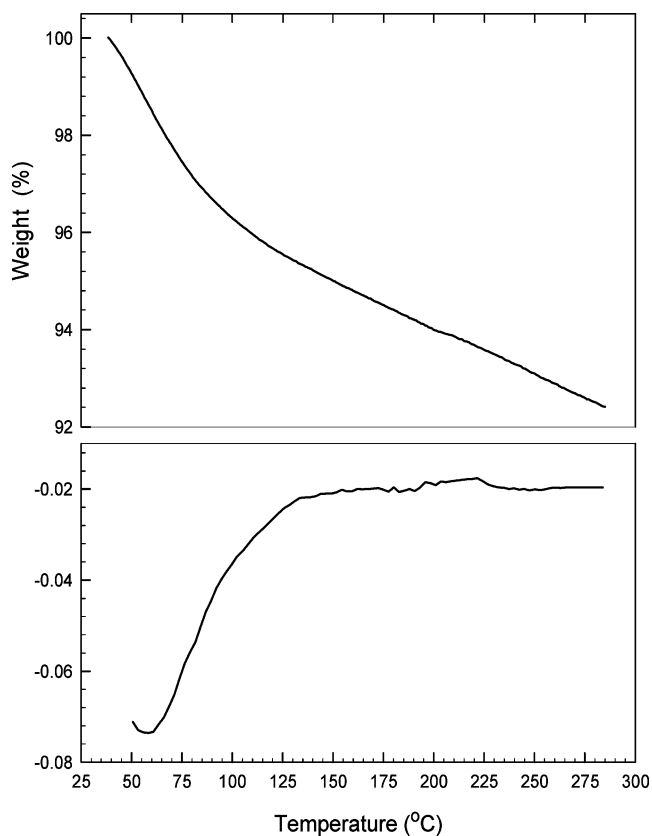


Figure 1. Thermogravimetric analysis of the anatase. The upper curve shows the weight loss as a function of temperature, and the lower curve is its derivative.

The adsorption/desorption isotherm for ST-01 exhibits hysteresis at high relative pressures characteristic of a mesoporous material (pore diameter between 2 and 50 nm). The isotherm can be identified as IUPAC Type IV/V with a hysteresis loop indicative of agglomerates containing spherical primary particles.⁵⁴ Pore size distribution and pore volume were calculated from the adsorption branch isotherm using the Barrett–Joyner–Halenda (BJH) method for cylindrical pore geometry.⁵⁵ Based on BJH analysis, two principal mesopore diameters are observed at about 3.4 and 9.5 nm. Using a theoretical density of 3.89 g/cm³ for anatase, the total porosity is estimated to be 70% for both adsorption and desorption branches.

High-Resolution Transmission Electron Microscopy. High-resolution TEM images of the anatase sample are shown in Figure 2. The anatase sample comprises monodisperse particles, with an average particle diameter of about 4 nm. The nanoparticles are subequant crystals, with visible facets and lattice patterns. The predominant crystal face, apparent from the lattice spacing, is the [101] plane. From the HR-TEM images, close-packed “primary” aggregates of the discrete crystallites are apparent. Within these “primary” aggregates there is evidence for alignment of adjacent grains along specific crystallographic planes, as neighboring particles are united by continuous crystal lattice lines. Similar close-packing of nanometer grains, with specific crystallographic orientations, was observed for 2 nm MgO particles by Mel’gunov et al.⁵⁶ The average primary particle size

(51) Almquist, C. B.; Biswas, P. *J. Catal.* **2002**, *212*, 145–156.

(52) Nosaka, A. Y.; Fujiwara, T.; Yagi, H.; Akutsu, H.; Nosaka, Y. *Chem. Lett.* **2002**, *3*, 420–421.

(53) Lowell, S.; Shields, J. E.; Thomas, M. A.; Thommes, M. *Characterization of porous solids and powders: surface area, pore size and density, Particle Technology Series*; Kluwer Academic Publishers: Boston, 2004; p 347.

(54) Zgrablich, G.; Mendioroz, S.; Daza, L.; Pajares, J.; Mayagoitia, V.; Rojas, F.; Conner, W. C. *Langmuir* **1991**, *7*, 779–785.

(55) Barret, E. P.; Joyner, L. G.; Halenda, P. P. *J. Am. Chem. Soc.* **1951**, *73*, 373–380.

(56) Mel’gunov, M. S.; Felonov, V. B.; Mel’gunova, E. A.; Bedilo, A. F.; Klabunde, K. J. *J. Phys. Chem. B.* **2003**, *107*, 2427–2434.

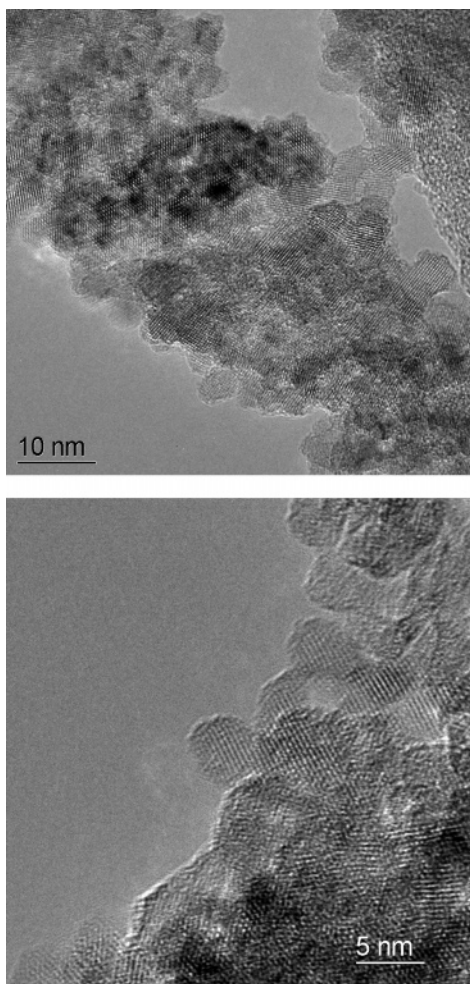


Figure 2. HR-TEM images of the nano-anatase sample with average particle diameter of 4 nm.

and the presence of closed-packed aggregates observed in the HR-TEM images correlate well with the SANS and USAXS results discussed below.

Scattering and Laser Diffraction Measurements. SANS and USAXS measurements yield similar scattering results for both the dry anatase powder and a 0.74% aqueous suspension of this powder, respectively (Figure 3). Vertical bars represent the estimated standard deviations for the measured scattered intensity values. The scattering data were analyzed using MaxEnt, an entropy maximization algorithm based on the MAXE.FOR code developed by Potton et al.⁵⁷ and modified by Jemian (see Jemian et al.⁵⁸). MaxEnt fits the scattering data by minimizing the fit error (determined by the chi-square statistic) while simultaneously maximizing the configurational entropy of the resulting scatterer size distribution; it thereby produces a solution with the minimal information necessary to explain the data. Of particular note, MaxEnt makes no assumptions with respect to the functional form of the distribution and is tolerant of discrete peaks that might otherwise be excessively smoothed by other regularization programs. In implementing this model we used a spheroid scattering form factor with an aspect ratio of 1. During the analysis, a flat incoherent background was estimated from the high- Q data and subtracted. The resulting distribution gives the differential volume fraction per Å diameter interval as a

(57) Potton, J. A.; Daniell, G. J.; Rainford B. D. *J. Appl. Crystallogr.* **1988**, *21*, 663–668.

(58) Jemian, P. R.; Weertman, J. R.; Long, G. G.; Spal, R. D. *Acta Metall. Mater.* **1991**, *39*, 2477–2487.

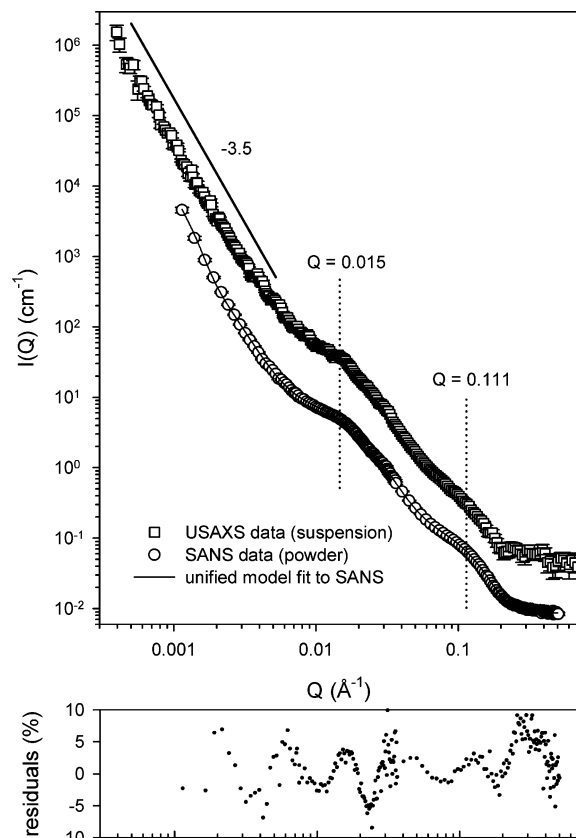


Figure 3. Scattering results for USAXS (0.74% aqueous suspension) and SANS (dry powder) measurements. A multilevel Guinier/power-law fit to the SANS data is included; the smaller graph at the bottom shows the residuals from this fit. Vertical bars, where visible, represent the absolute standard deviation of the scattered intensity. To improve visibility, the SANS data have been vertically scaled.

function of the diameter. The MaxEnt analysis yielded two primary size distribution modes: a sharp peak centered at 3.7 nm and a broad mode at about 11.5 nm (Figure 4). The finer size peak constitutes 74% and 62% of the detectable volumetric size distribution for the powder and suspension, respectively. The USAXS data shows a steeply rising intensity at low Q values, which suggests the presence of larger-scale structural heterogeneities approaching the micrometer range, though this is not reflected in the MaxEnt results.

A log–log plot of the USAXS data yields a power-law region with a slope of -3.5 at low Q values (Figure 3). A power-law exponent between 3 and 4 is often attributed to surface fractal scattering,⁵⁹ with fractal dimension $D_s = 2.55$ (slope = $-(6 - D_s)$); alternatively, it could be attributed to a power-law distribution of pore sizes. In contrast, a sharp (nonfractal) surface would be characterized by $D_s = 2$ and would produce Porod power-law scattering with a characteristic exponent of -4 . The Q range of the SANS data was too limited for a complete analysis; nevertheless, a steeply increasing intensity was also suggested at low Q .

Both SANS and USAXS data display maxima near $Q = 0.015 \text{ \AA}^{-1}$ and 0.111 \AA^{-1} , although the higher- Q feature is poorly defined in the USAXS curve because of the higher incoherent scattering background in that region (Figure 3). These features can be interpreted as interference (Bragg-like) peaks representing ordering at length scales $2\pi/Q$ of roughly 42.5 and 5.6 nm, respectively. This type of feature is often associated with close-packed particle structures. Note that the smaller length scale is

(59) Bale, H. D.; Schmidt, P. W. *Phys. Rev. Lett.* **1984**, *53*, 596–599.

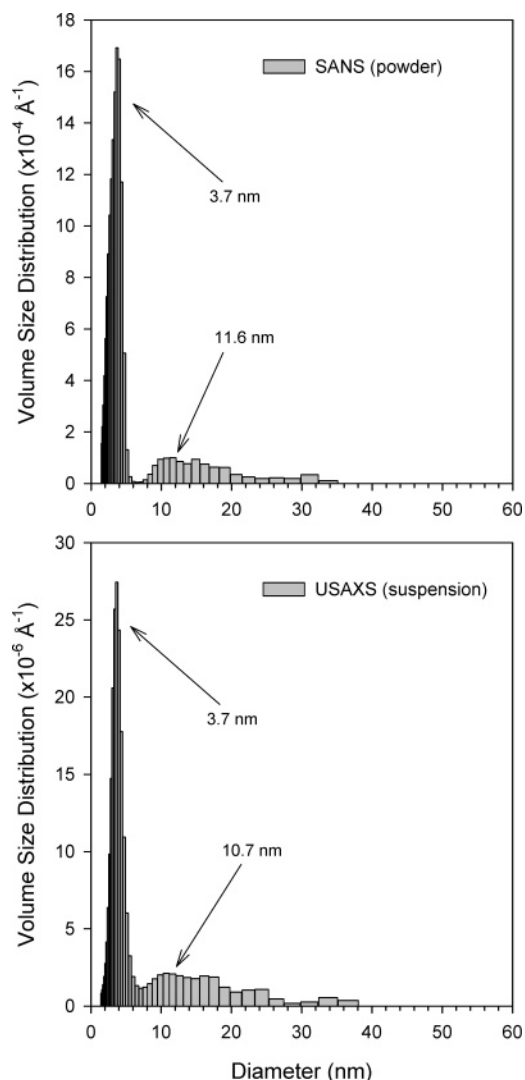


Figure 4. Analysis of SANS (top) and USAXS (bottom) data using a maximum entropy method with a spherical form factor. Principal particle size modes of 3.7 and 11.5 nm are indicated.

close to the reported value for the diameter of the primary crystallites (about 4 nm). The larger value may reflect “primary” clusters of the smallest crystallites, which are themselves packed into larger-scale aggregates resulting in a hierarchical multiscale structure.

An alternate interpretation of the scattering invokes multiple Guinier exponential scattering regions for characteristic particle sizes separated by fractal-like power-law regions associated with underlying aggregate structures. This interpretation assumes the existence of a structural hierarchy within the material. Using the unified Guinier/power-law model of Beaucage,⁶⁰ the SANS data were fit with three such structural levels each characterized by a radius of gyration (R_g) and underlying fractal scaling regime. The SANS data yielded characteristic diameters ($2a$) of 550, 27, and 4.2 nm (for spherical particle geometry, $R_g = 0.775a$, where a is the sphere radius). The first value is unreliable, since it was estimated in order to provide a good fit to the low- Q data; the largest scale Guinier region is not observable in the measured Q range, but the estimate suggests the presence of large aggregates. The second and third diameter values correlate with the MaxEnt results. The corresponding power-law coefficients derived from the unified fit are less informative, since these regions are poorly

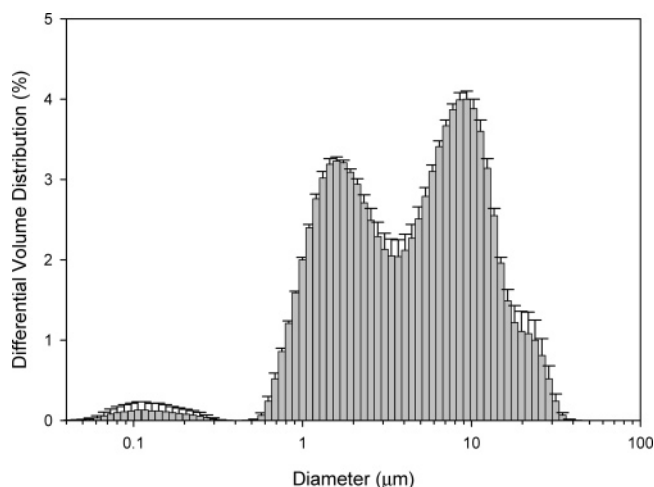


Figure 5. Laser diffraction derived mean differential volumetric size distribution for anatase suspensions shows the predominance of microscale aggregates. ST-01 was dispersed in deionized water adjusted to pH 2.7.

developed in the SANS data, but they are consistent with an interpretation of three or more connected structural levels constructed from primary crystallites and their larger-scale assemblies.

Laser diffraction analysis of suspensions prepared under conditions close to those used in the titration experiments, but at a lower solid phase concentration, indicate that ST-01 exists mostly as microscale aggregates in suspension, with the bulk of the material falling in the range between about 1 μm and 30 μm (Figure 5) and with a relatively small mode centered near 100 nm. Integration of the volume distribution curve shows that 99.96% of the distribution volume is characterized by diameters larger than 400 nm. Even with conversion from volume- to number-weighting, most of the material remains in the micrometer range. These aggregates do not easily break apart when dispersed in water under conditions that should otherwise facilitate the formation of a stable TiO_2 suspension (low pH and low ionic strength, application of disruptive energy from ultrasonic cavitation). Application of additional ultrasonic energy did not significantly alter the measured size distribution.

The HR-TEM, laser diffraction and small-angle scattering results, collectively, indicate that the anatase sample comprises primary crystallites of about 4 nm diameter. These particles are then assembled into larger clusters that exhibit a hierarchical structure. A second characteristic length-scale in the (30 to 40) nm range may constitute close-packed clusters with the primary crystallites orientated along specific crystallographic planes. Larger structures appear to exist that are characterized by a fractal surface geometry or pore structure, but appear to be homogeneous internally. These microscale structures are probably large aggregates of the smaller clusters and primary particles. All of these structures appear largely stable when dispersed in an aqueous suspension, even under intense ultrasonic treatment. This suggests that very little of the material mass exists as independent primary particles, either in the dry powder form or in aqueous dispersion.

Titration Results

Experimental Considerations. The titration of nanosized particles introduced several experimental considerations that are typically of minimal concern when titrating macroscopic particles. Most importantly, it was necessary to ensure that the surface titration results reflected the reactivity of the entire surface area of the primary crystallites and not just the surface of the close-

(60) Beaucage, G. J. *Appl. Crystallogr.* **1995**, *28*, 717–728.

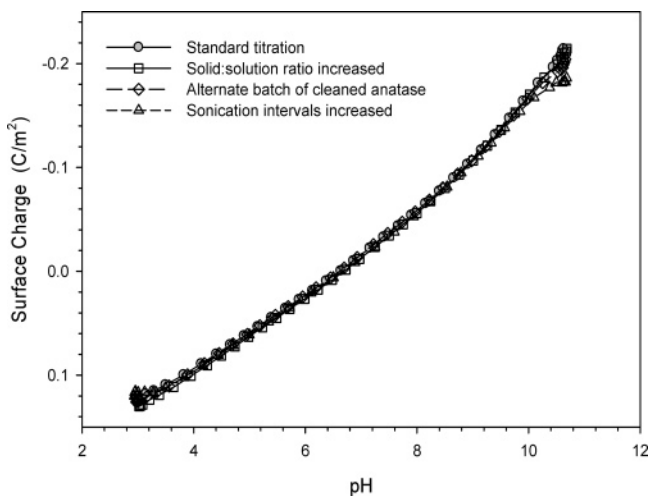


Figure 6. The effect of varying the experimental parameters on net proton charge curves for anatase at 25 °C and 0.3 *m* ionic strength are shown. In one titration the solid:solution ratio was increased by 30%, whereas in a second titration the sonication interval was increased. In the second batch of cleaned anatase the surface area was 310 m²/g.

packed aggregates. The scattering and laser diffraction measurements indicated that even following intense ultrasonication the anatase aggregates were not entirely dispersed as primary particles. However, the sonication procedure appeared to open up the aggregates, permitting wetting of all surfaces, as well as allowing these surfaces to respond rapidly and reproducibly during titration. Titrations completed following sonication were reproducible; moreover, the cell potential equilibrated quickly and remained stable, which was not the case when the dispersion step was omitted or inadequate. The sonication procedure did not impact the titration results or adversely alter the nanoparticles, as reproducible titrations were obtained when varying the dispersion procedure (Figure 6). For example, Figure 6 shows the titration results of varying the duration of cavitation; in addition, other experimental parameters were also varied, all producing identical titration results. Experimental parameters varied, included increasing the intensity of cavitation, decreasing the interval but increasing the number of cycles of ultrasonication, varying the solid:solution ratio, using different batches of cleaned anatase sample, etc. (Figure 6).

Standard deviation of the surface charge values was determined from the replicate titration data presented in Figure 6. On all surface titration plots, one standard deviation was smaller than the data symbols, except at very low and high pH values (3 > pH > 10). In addition, the replicate titration data in Figure 6 were combined and fitted with a third-order polynomial equation, for which the resulting *R*² value exceeded 0.99.

As described earlier, in all potentiometric titrations a Ross combination glass electrode was used; these electrodes comprise porous ceramic reference junctions. Although there was no evidence that the anatase nanoparticles clogged or diffused through the ceramic junction, titrations were completed using a Ross Sure-flow electrode to verify this. The Ross Sure-flow electrodes are specifically designed for pH measurements of colloidal samples and have a liquid-to-liquid junction that eliminates potential clogging. Furthermore, to maximize any potential liquid junction effects, the titrations completed using the Ross Sure-flow electrode were performed at 0.3 *m* ionic strength (i.e., the highest ionic strength used in this study). The surface titration results of the two electrodes were identical. As anticipated, the calculated liquid junction potential of the Sure-

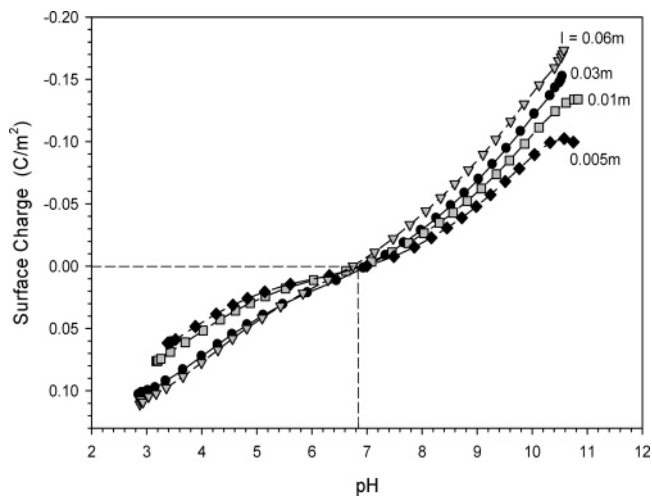


Figure 7. Net proton charge curves for anatase at 25 °C in NaCl media at varying ionic strengths. The dashed vertical line represents the chosen pH_{znp} value of 6.85 at zero net proton charge (horizontal line).

flow electrode was slightly higher than the liquid junction potential of the combination electrode.

Potentiometric Titration Results. The net proton charge curves of ST-01 at varying ionic strengths are shown in Figure 7. The titrations performed at ionic strengths of 0.06 *m* and less exhibit a common intersection point at zero surface charge and a pH of 6.85. This intersection point defines the zero net proton charge (pH_{znp}) value; however, a pH_{znp} value of 6.85 is higher than most previously reported values for macroscopic anatase. Kosmulski⁶¹ and Bourikas et al.⁶² report median pH_{znp} and/or pH_{iep} values of 6.2 to 6.3 for anatase, based on earlier literature results. Moreover, for those studies where pH_{znp} and pH_{iep} values were both determined and agree, Kosmulski⁶³ reports an average pH_{znp/iep} value of 5.9 for both rutile and anatase. There are only a few previously reported pH_{znp} or pH_{iep} values for nanocrystalline anatase (*d* < 20 nm). Kormann et al.⁶⁴ reported a pH_{zpc} of 5.1 (± 0.2) for a nanocrystalline anatase with an average particle diameter < 3 nm, and pH_{znp} and pH_{iep} values of 5.8 were determined for a 6 nm average diameter specimen.^{65–67}

Figure 8 compares the proton charge curves for ST-01 anatase to those of a rutile sample with a much larger primary crystallite size (0.5 μm), relative to the respective pH_{znp} values of these samples (5.4 for rutile). Both negative (pH_{znp} – pH < 0) and positive (pH_{znp} – pH > 0) surface charge development for ST-01 anatase is similar to that of larger rutile crystallites, which indicates the Na⁺ and Cl[–] counterions screen surface charge development similarly for these solids. Moreover, the proton-induced surface charge is asymmetric about the pH_{znp} value: the slopes of the titration curves are steeper above the pH_{znp} value than below. Additionally, at higher ionic strengths, (0.06 and 0.3 *m*), there is a subtle but distinct shift in the apparent pH_{znp} value toward lower pH. At 0.3 *m* ionic strength the apparent pH_{znp} value is 6.62, approximately 0.2 pH units below the

(61) Kosmulski, M. *Chemical Properties of Material Surfaces. Surfactant Science Series*; Marcel Dekker: New York, 2001; Vol. 102.

(62) Bourikas, K.; Hiemstra, T.; Van Riemsdijk, W. H. *Langmuir* **2001**, *17*, 749–756.

(63) Kosmulski, M. *Adv. Colloid Interface Sci.* **2002**, *99*, 255–264.

(64) Kormann, C.; Bahnmann, D. W.; Hoffmann, M. R. *J. Phys. Chem.* **1988**, *92*, 5196–5201.

(65) Jing, C.; Meng, X.; Liu, S.; Baidas, S.; Patraju, R.; Christodoulatos, C.; Korfiatis, G. P. *J. Colloid Interface Sci.* **2005**, *290*, 14–21.

(66) Pena, M. E.; Korfiatis, G. P.; Patel, M.; Lippincott, L.; Meng, X. *Water Res.* **2005**, *39*, 2327–2337.

(67) Pena, M. E.; Meng, X.; Korfiatis, G. P.; Jing, C. *Environ. Sci. Technol.* **2006**, *40*, 1257–1262.

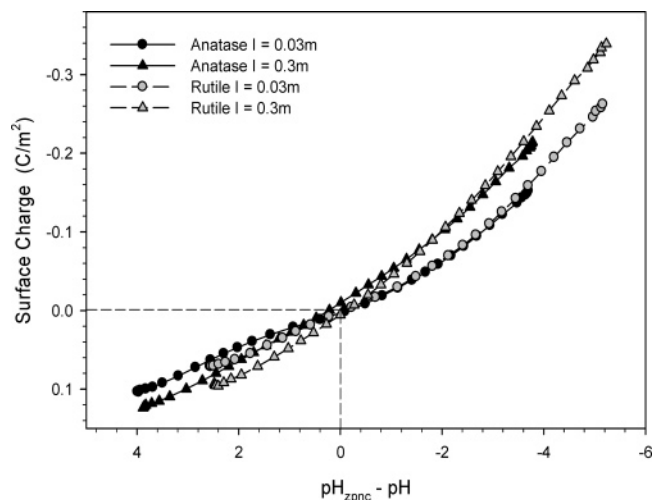


Figure 8. Net proton charge curves for anatase and rutile relative to their respective pH_{znpc} values of 6.85 and 5.4. The anatase particles were 4 nm in diameter, whereas the rutile sample comprised much larger primary crystallite particles of 0.5 μm . All titrations were completed at 25 $^{\circ}\text{C}$ in NaCl media.

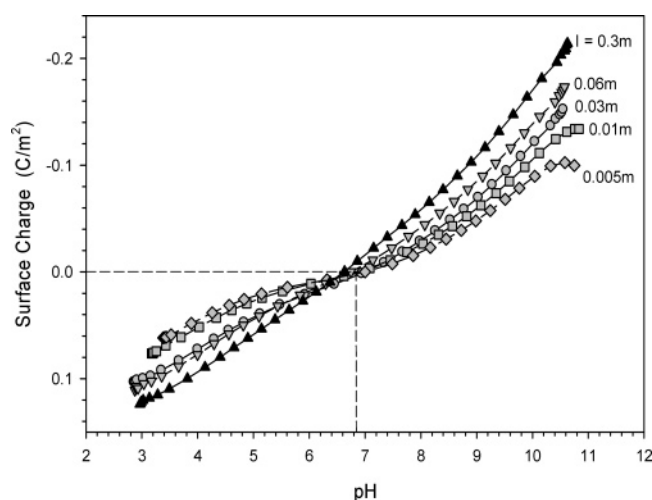


Figure 9. Net proton charge curves for anatase showing a subtle shift in the apparent pH_{znpc} at 0.3 m ionic strength (\blacktriangle), at 25 $^{\circ}\text{C}$ in NaCl media. The dashed vertical line represents the chosen pH_{znpc} value of 6.85 at zero net proton charge (horizontal line).

common intersection point of the lower ionic strength titration curves (Figure 9). Together, these results may be attributed to the Na^+ ions approaching the surface more closely than the much larger Cl^- ions and/or a greater intrinsic affinity between the TiO_2 surface and Na^+ ions. In particular, the apparent decrease in the pH_{znpc} value with increasing electrolyte concentration suggests that the Na^+ ions are specifically adsorbed to some extent at these surfaces, whereas the larger Cl^- ions are not. That so-called “inert” electrolyte cations can adsorb specifically has been demonstrated conclusively for single-crystal rutile [110] surfaces,³³ and the [110] crystal face dominates the rutile powder depicted in Figure 8.²⁹ Apparently, Na^+ may also be specifically adsorbing on ST-01 anatase which is dominated by the [101] crystal face (Figure 2).

Electrokinetic Measurements. The electrophoretic mobility titration data and five-parameter sigmoid fits are presented in Figure 10. The mean pH_{iep} value at all ionic strengths is 6.84, which is in exceptional agreement with the pH_{znpc} value of 6.85 obtained from the potentiometric titration data (Figure 9). Unlike the potentiometric titration data, no shift in the pH_{iep} value at 0.3 m ionic strength was observed. At high ionic strengths, one would

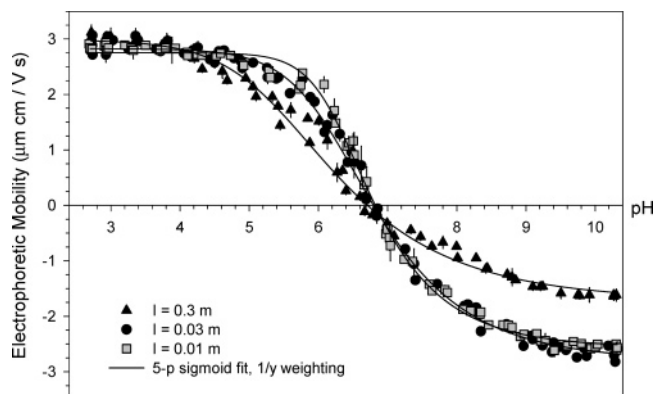


Figure 10. Electrophoretic mobility titration curves as a function of pH at 25 $^{\circ}\text{C}$, in NaCl media. The curves represent five-parameter sigmoid (logistic) fits with a 1/y weighting.

anticipate an increase in the isoelectric point pH value corresponding to the observed decrease in apparent pH_{znpc} value, which was assumed to indicate specific adsorption of Na^+ ions at high electrolyte loading. However, higher ionic strengths ($>0.3 m$ NaCl) may be necessary to cause a comparable shift in the pH_{iep} .^{68,69} Nevertheless, the excellent agreement between the pH_{iep} and the pH_{znpc} values suggests that these values equate to a pristine point of zero charge (pH_{ppzc}) of 6.85, for ST-01 anatase.

The maximum zeta potentials (determined at the low-pH plateau) for ST-01 at each NaCl molality are reported in Table 2. OW calculations were corrected for the additional contribution of protons to the solution ionic conductance at low pH, using a molar weighting of Na^+ and H^+ . Results for the as-received ST-01 powder (i.e., not subject to the cleaning procedure previously described) are also included for comparison. Because it is possible to calculate different potentials depending on the assumptions made regarding the appropriate physical model and interface of the particles, the Smoluchowski and OW results effectively define upper and lower limits for the plateau potential, lying between about 36 mV and 60 mV for all molalities. Data for the cleaned versus as-received powder suggests that ST-01 is largely free of specifically adsorbed surface ionic species. The Smoluchowski and OW results also exhibit a surprising insensitivity of the plateau potential to salt concentration, with all values lying within less than 3 mV of each other for a given calculation method.

Taking into account the porous aggregate structure of ST-01, and applying the theoretical treatment of Miller–Berg–O’Brien (MGO) using a pore volume fraction of 0.7,⁴⁹ calculated potentials at each NaCl molality fall between the Smoluchowski and OW values (see Table 2). Calculations show that as the salt concentration, and hence κa , increases, the reduction in EDL overlap within the pore channels leads to an increase in the intraaggregate electroosmotic flow. This partially compensates for the decrease in mobility induced by the presence of conducting fluid inside the aggregate pore volume. MGO results suggest that the Smoluchowski formula for large κR , where R is the external aggregate radius, underestimates the actual potential by as much as 21% at the lowest NaCl molality. The MGO analysis also recovers a small but systematic decrease in potential with increasing salt concentration, as would be expected based on simple charge screening (partly compensated by the greater surface charge density permitted with increasing salt concentration; see e.g., Figure 9). It should be noted that the specific pore

(68) Breeuwsma, A.; Lyklema, J. *J. Colloid Interface Sci.* **1973**, *43*, 437–448.

(69) Hiemstra, T.; Yong, H.; Van Riemsdijk, W. H. *Langmuir* **1999**, *15*, 5942–5955.

Table 2. Maximum Zeta Potential Values for ST-01 Determined from the Low-pH Plateau Region of the Mobility Titrations as a Function of NaCl Molality and Method of Calculation^a

	zeta potential (mV)			
	0.01 mol/kg NaCl, $\kappa a = 0.8$	0.03 mol/kg NaCl, $\kappa a = 1.29$	0.03-AR mol/kg NaCl, $\kappa a = 1.29$	0.3 mol/kg NaCl, $\kappa a = 4.0$
Smoluchowski	36.6 ± 0.6	36.8 ± 1.7	37.0 ± 1.3	39.1 ± 0.5
Porous Aggregate	46.5 ± 0.7	44.9 ± 2.1	45.1 ± 1.6	41.4 ± 0.6
O'Brien-White	58.6 ± 1.0	58.9 ± 3.3	59.4 ± 2.6	59.9 ± 1.1

^a A primary particle radius of 2.2 nm was used to determine κa . (AR = as-received powder, i.e., not subjected to cleaning procedure).

volume determined from BJH analysis of the gas adsorption isotherm may include some mesoporosity that exists only in the dry powder state (i.e., interaggregate porosity) and thus may overestimate the dispersed phase aggregate porosity. As the relative pore volume decreases, the calculated mobility will approach the Smoluchowski limit. We further note that the calculated potentials are a bit higher than the theoretical application limit of 25 mV for the MGO model⁵⁰ (corresponding to the Debye–Hückel regime), but they are not exceedingly high, and the model should therefore provide a reasonable estimate for the effect of porosity. On the other hand, the choice of model is inconsequential with respect to the determination of the IEP.

Conclusions

By combining the detailed surface titrations and characterization results presented here, we can start to elucidate the surface reactivity of metal-oxide nanoparticles in aqueous solutions. Specifically from this study, it is apparent that classic titration procedures utilized routinely to investigate the surface charging properties of metal-oxide particles can also provide comparable information for the surface charging properties of nanoparticles. However, a few modifications to these normal titration procedures were found to be necessary to ensure reproducible titrations. First, aggressive solid pretreatment procedures must be avoided. For example, even relatively mild elevated heat treatments such as boiling in deionized water lead to noisy and irreproducible titration results. Second, ultrasonic dispersion, immediately preceding titration, was found to significantly improve titration reproducibility, presumably by enhancing particle dispersion. Still, even following ultrasonic treatment, the primary crystallites existed almost exclusively in a hierarchy of agglomerated structures. Gas adsorption/desorption hysteresis indicates ST-01 is mesoporous, with a pore volume fraction of roughly 70%.

The potentiometric and electrophoretic mobility titration results for ST-01 were in excellent agreement, with both the pH_{znpc} and pH_{iep} values being 6.85 (± 0.02). However, the shift in the pH_{znpc} to lower pH values in 0.3 *m* NaCl (about pH 6.6) suggests that some specific adsorption of the Na^+ ions occurs at higher ionic strengths. Specific adsorption of so-called “inert” electrolyte

has been demonstrated previously on macroscopic rutile³³ but only at even higher ionic strengths (≥ 1.0 *m*), as is also suggested by Figure 8 where no pH_{znpc} shift is apparent for macroscopic rutile in 0.3 *m* NaCl. Despite this rather subtle difference, the charging curves of ST-01 anatase are very similar to the more macroscopic rutile form of TiO_2 despite these crystallites being dominated by different crystal planes ([101] and [110], respectively). In any case, the charging and electrophoretic mobility properties of nanocrystalline anatase will be explored more quantitatively with the aid of surface complexation models.

Acknowledgment. This research was funded by NSF under the NIRT initiative (EAR-0124001). The HR-TEM characterization was completed with the help of Drs. Larry Allard and Jane Howe, Oak Ridge National Laboratory, High Temperature Materials Laboratory User Program and the Center for Nanophase Materials Sciences, managed by UT-Battelle, LLC, for the U.S. Department of Energy (DOE) under contract number DE-AC05-00OR22725. The UNICAT facility at the Advanced Photon Source (APS) is supported by the U.S. DOE under Award No. DEFG02-91ER45439, through the Frederick Seitz Materials Research Laboratory at the University of Illinois at Urbana-Champaign, the Oak Ridge National Laboratory (U.S. DOE contract DE-AC05-00OR22725 with UT-Battelle LLC), the National Institute of Standards and Technology (U.S. Department of Commerce), and UOP LLC. The APS is supported by the U.S. DOE, Basic Energy Sciences, Office of Science, under contract No. W-31-109-ENG-38. We thank Professor Michio Matsumura of Osaka University for help in obtaining the ST-01 sample. We also thank Andrew Allen (NIST) and Pete Jemian (APS), who were instrumental in obtaining the USAXS data. The NIST Center for Neutron Research is acknowledged for access to the NG-7 neutron beam line, and Derek Ho is thanked for his help with the SANS measurements. V.A.H. acknowledges support for this work by a NIST Materials Science and Engineering Laboratory Director's Reserve award, and M.L.M. acknowledges the support of the Illinois State Water Survey and Illinois Department of Natural Resources.

LA061774H